

Non-abelian Dark Matter Solutions for Galactic Gamma-ray Excess and Perseus 3.5 keV X-ray Line

KINGMAN CHEUNG^{a,b,1}, WEI-CHIH HUANG^{c,2}, YUE-LIN SMING TSAI^{d,3}

^a *Department of Physics, National Tsing Hua University, Hsinchu 300, Taiwan*

^b *Division of Quantum Phases and Devices, School of Physics, Konkuk University, Seoul 143-701, Republic of Korea*

^c *Department of Physics and Astronomy, University College London, UK*

^d *Kavli IPMU (WPI), The University of Tokyo, Kashiwa, Chiba 277-8583, Japan*

Abstract

We attempt to explain simultaneously the Galactic center gamma-ray excess and the 3.5 keV X-ray line from the Perseus cluster based on a class of non-abelian $SU(2)$ DM models, in which the dark matter and an excited state comprise a “dark” $SU(2)$ doublet. The non-abelian group kinetically mixes with the standard model gauge group via dimensions-5 operators. The dark matter particles annihilate into standard model fermions, followed by fragmentation and bremsstrahlung, and thus producing a continuous spectrum of gamma-rays. On the other hand, the dark matter particles can annihilate into a pair of excited states, each of which decays back into the dark matter particle and an X-ray photon, which has an energy equal to the mass difference between the dark matter and the excited state, which is set to be 3.5 keV. The large hierarchy between the required X-ray and γ -ray annihilation cross-sections can be achieved by a very small kinetic mixing between the SM and dark sector, which effectively suppresses the annihilation into the standard model fermions but not into the excited state.

¹cheung@phys.nthu.edu.tw

²wei-chih.huang@ucl.ac.uk

³yue-lin.tsai@ipmu.jp

1 Introduction

A gamma-ray excess around a few GeV near the Galactic center (GC) region, seen by the Fermi-LAT collaboration (see, for instance, the recent analysis by the collaboration [1]), has been widely discussed based on dark matter (DM) annihilations into standard model (SM) fermions [2–15], which hadronize into neutral pions followed by $\pi^0 \rightarrow \gamma\gamma$, or electromagnetic bremsstrahlung. On the other hand, recent reports of the 3.5 keV X-ray line [16, 17] from the XMM-Newton data have triggered many studies in the context of DM, for example, Refs. [18–65]. Roughly speaking, they can be classified into two categories: (i) DM undergoes upscattering into an excited state followed by the decay back into DM and an X-ray photon; and (ii) decaying DM matter, such as a 7 keV sterile neutrino decaying into an active neutrino and the X-ray photon. The excited DM, however, has an advantage of explaining some null results on X-ray line searches due to a low local DM velocity as shown in Ref [66].

There is a very interesting connection between the γ -ray excess and X-ray line as follows. The GC γ -ray excess can be explained by annihilating DM with a mass from 10 to 60 GeV [2, 5–8, 10–12], depending on the final state of the annihilation. On the other hand, due to the fact that the current DM velocity is around $10^{-3}c$ in the Perseus cluster, where the X-ray line is observed, the DM with a mass of 10 to 60 GeV coincidentally has a kinetic energy of a few keV. It implies if there exists an excited state with a 3.5 keV mass splitting from the DM particle, then the DM particles can annihilate into the excited state, followed by the decay back into the DM particle with a photon accounting for the observed X-ray line.

In this work, we employ a class of non-abelian $SU(2)_X$ DM models proposed in Refs. [18, 67], where the DM particle and the excited state form an $SU(2)_X$ doublet with a 3.5 keV mass splitting. The $SU(2)_X$ kinetically mixes with the SM gauge group via dimension-5 operators, through which the SM particles can couple to the $SU(2)_X$ currents and the DM (and the excited state) couples to the SM currents. As mentioned above, the GC γ -ray excess comes from the DM annihilation into SM fermions accompanied by photon emission while the X-ray line is realized from the DM annihilation into the excited state followed by the subsequent decay. Besides, the annihilation into SM fermions, induced by the kinetic mixing, is suppressed compared to that into the excited state if the kinetic mixing is small. This suppression naturally explains the hierarchy between the required annihilation cross-sections for the γ -ray excess ($10^{-26} \text{ cm}^3\text{sec}^{-1}$) and the X-ray line emission ($10^{-19} \text{ cm}^3\text{sec}^{-1}$) as shown below. Note that similar ideas connecting the γ -ray and X-ray excess have been suggested in Refs. [18, 39] with intermediate states (instead of the SM fermion final state) while an effort connecting the 511 keV line [68] and the GC γ -ray excess turns out to be negative [69].

This paper is organized as follows. In Sec. 2, we specify the model and divide into the Majorana and Dirac DM cases. In Sec. 3, we calculate the relevant cross-sections. In Sec. 4, we discuss the calculations of γ -ray and X-ray flux as well as the DM relic abundance. In Sec. 5, we present our numerical analysis with separation into the Majorana and Dirac cases. Finally, we conclude in Sec. 6.

2 Non-abelian Dark Matter Models

For the nonabelian DM model, we employ a “dark” $SU(2)_X$ gauge group with kinetic mixing with the SM gauge groups proposed in Refs. [18,67]. We start with a $SU(2)_X$ doublet, which is comprised of the fields for the DM particle and an excited state. In the following we will discuss two cases: (i) Majorana DM (χ_1) with the Dirac excited state (ψ_2) and (ii) Dirac DM (ψ_1) with the Dirac excited state (ψ_2).¹ As we shall see later, we have to make use of the resonance enhancement in order to achieve large annihilation cross-sections, especially for explaining the X-ray line. The resonance enhancement does not occur if both DM and the excited state are Majorana with nearly degenerate masses, as shown in Appendix A. On the other hand, the Dirac DM with the Majorana excited state will lead to a large γ -ray flux but a small X-ray one, in contradiction to the γ -ray and X-ray data. Therefore, we will not discuss these two scenarios in this work. The Lagrangian of the model reads,

$$\mathcal{L} = \mathcal{L}_{SM} + \mathcal{L}_{DM_1} + \mathcal{L}_{DM_2} + \mathcal{L}_{mix}, \quad (2.1)$$

where \mathcal{L}_{SM} is the SM Lagrangian. $\mathcal{L}_{DM_{1,2}}$ correspond to the DM sector, including the DM doublet and the dark $SU(2)$ gauge bosons, X^a ($a = (1, 2, 3)$), and dark Higgs triplets/doublets, which are used to provide masses to χ s and X s:

$$\mathcal{L}_{DM_1} = -\frac{1}{4}X^{\mu\nu a}X_{\mu\nu}^a + (D_\mu^X \Delta_1)^\dagger (D_\mu^X \Delta_1) + (D_\mu^X \Delta_2)^\dagger (D_\mu^X \Delta_2), \quad (2.2)$$

where D_μ^X is the covariant derivative of $SU(2)_X$ and $\Delta_{1,2}$ are $SU(2)$ triplets, whose vacuum expectation values (VEVs) provide masses to dark gauge bosons. Note that one can play with the structure of $\langle \Delta_i \rangle$ to give different masses to X^a . For example, with $\langle \Delta_2 \rangle = (0, v, 0)^T$ in the isospin basis (the first component has the highest isospin $I_3^X = 1$, the second with $I_3^X = 0$, and so on) $X^{1,2}$ are massive but X^3 remains massless.

2.1 Majorana DM

In the case of Majorana DM, the \mathcal{L}_{DM_2} takes the form

$$\mathcal{L}_{DM_2} = i\chi^\dagger D_\mu^X \sigma^\mu \chi + i\tilde{\chi}_2^\dagger \partial_\mu \bar{\sigma}^\mu \tilde{\chi}_2 + \left(\frac{1}{2} \lambda_\Delta (\chi \cdot \Delta_1 \cdot \chi) + \lambda_{h_2} (\chi \cdot h_D) \tilde{\chi}_2 + h.c. \right), \quad (2.3)$$

where the two-component Weyl spinor notation is employed. Here “ \cdot ” refers to the $SU(2)$ -invariant multiplication. χ is an $SU(2)_X$ doublet, consisting of two Weyl spinors, χ_1 and χ_2 : $\chi = (\chi_2 \ \chi_1)^T$. In addition, h_D is an $SU(2)_X$ scalar doublet. $\tilde{\chi}_2$ is a singlet under $SU(2)_X$, which will be paired up with χ_2 to form a Dirac fermion. The conversion between Dirac- and

¹In this work, we denote Majorana particles by χ and Dirac particles with ψ for particles in the dark sector.

Weyl-spinors for χ_1 , χ_2 and $\tilde{\chi}_2$ is:

$$\begin{aligned}\psi_1 &= \begin{pmatrix} \chi_1 \\ \chi_1^\dagger \end{pmatrix}, \\ \psi_2 &= \begin{pmatrix} \chi_2 \\ \tilde{\chi}_2^\dagger \end{pmatrix}.\end{aligned}\tag{2.4}$$

The corresponding X^3 -current in the Weyl and Dirac-spinor notation is given by

$$\begin{aligned}\mathcal{L} &\supset g_X X_\mu^3 J_X^\mu = -\frac{g_X}{2} X_\mu^3 \chi_1^\dagger \bar{\sigma}^\mu \chi_1 + \frac{g_X}{2} X_\mu^3 \chi_2^\dagger \bar{\sigma}^\mu \chi_2 \\ &= -\frac{g_X}{2} X_\mu^3 \bar{\psi}_1 \gamma^\mu \left(-\frac{\gamma^5}{2}\right) \psi_1 + \frac{g_X}{2} X_\mu^3 \bar{\psi}_2 \gamma^\mu \left(\frac{1-\gamma^5}{2}\right) \psi_2,\end{aligned}\tag{2.5}$$

where the pre-factors $\pm 1/2$ come from the fact that $\chi_{2(1)}$ has $SU(2)_X$ isospin $1/2$ ($-1/2$).

In order to give a Majorana mass to χ_1 , one can make use of the lowest isospin ($I_3^X = -1$) component of $\langle \Delta_1 \rangle$, leaving VEVs of other components vanishing, i.e., $\langle \Delta_1 \rangle = (0, 0, v_{-1})^T$ in the isospin basis. The χ_1 mass becomes $\lambda_\Delta v_{-1}$. Similarly, with the lower isospin ($I_3 = -1/2$) of $\langle h_D \rangle$, the Dirac mass of χ_2 and $\tilde{\chi}_2$ becomes $\lambda_h v_{-1/2}$, where $v_{-1/2}$ is the VEV of the component of $I_3^X = -1/2$. Moreover, X^a 's masses, at phenomenological level, are considered independent since as mentioned above one can always use $\langle \Delta_2 \rangle$ to give a mass to specific gauge boson(s).

The particle content in the dark sector and the relevant quantum numbers in this model are summarized in Table 1.

| Field | $\Delta_{1,2}$ | h_D | χ | $\tilde{\chi}_2$ | $X^{1,2,3}$ |
|-----------|----------------|-------|--------|------------------|-------------|
| $SU(2)_X$ | 3 | 2 | 2 | 1 | 3 |
| spin | 0 | 0 | 1/2 | 1/2 | 1 |

Table 1: *The particle content and quantum numbers in the dark sector for the Majorana case.*

We would like to point out that the VEVs of $\Delta_{1,2}$ and h_D are used to give a mass to the particles of interest and induce the kinetic mixing between the SM and the dark sector. We simply assume that they are very heavy and play no roles in the context of GC gamma ray excess and the 3.5 keV X-ray line.

2.2 Dirac DM

In the case of Dirac DM, the \mathcal{L}_{DM_2} takes the form

$$\mathcal{L}_{DM_2} = i\chi^\dagger D_\mu^X \sigma^\mu \chi + \sum_{i=1}^2 i\tilde{\chi}_i^\dagger \partial_\mu \bar{\sigma}^\mu \tilde{\chi}_i + (\lambda_{h_1} (\chi \cdot h_{D_1}) \tilde{\chi}_1 + \lambda_{h_2} (\chi \cdot h_{D_2}) \tilde{\chi}_2 + h.c.), \tag{2.6}$$

where $\langle h_{D_1} \rangle = (v_1, 0)^T$ ($\langle h_{D_2} \rangle = (0, v_2)^T$) gives a Dirac mass to χ_1 and $\tilde{\chi}_1$ (χ_2 and $\tilde{\chi}_2$). We list the particle content and quantum numbers in Table 2. The conversion between Dirac- and Weyl-spinors for χ_1 , χ_2 and $\tilde{\chi}_2$ is:

$$\begin{aligned}\psi_1 &= \begin{pmatrix} \chi_1 \\ \tilde{\chi}_1^\dagger \end{pmatrix}, \\ \psi_2 &= \begin{pmatrix} \chi_2 \\ \tilde{\chi}_2^\dagger \end{pmatrix},\end{aligned}\tag{2.7}$$

and the corresponding X^3 -current in the Weyl and Dirac-spinor notation is

$$\begin{aligned}\mathcal{L} &\supset g_X X_\mu^3 J_X^\mu = -\frac{g_X}{2} X_\mu^3 \chi_1^\dagger \bar{\sigma}^\mu \chi_1 + \frac{g_X}{2} X_\mu^3 \chi_2^\dagger \bar{\sigma}^\mu \chi_2 \\ &= -\frac{g_X}{2} X_\mu^3 \bar{\psi}_1 \gamma^\mu \left(\frac{1 - \gamma^5}{2} \right) \psi_1 + \frac{g_X}{2} X_\mu^3 \bar{\psi}_2 \gamma^\mu \left(\frac{1 - \gamma^5}{2} \right) \psi_2.\end{aligned}\tag{2.8}$$

| Field | $\Delta_{1,2}$ | $h_{D_{1,2}}$ | χ | $\tilde{\chi}_{1,2}$ | $X^{1,2,3}$ |
|-----------|----------------|---------------|--------|----------------------|-------------|
| $SU(2)_X$ | 3 | 2 | 2 | 1 | 3 |
| spin | 0 | 0 | 1/2 | 1/2 | 1 |

Table 2: *The particle content and quantum numbers for the Dirac case.*

2.3 Kinetic Mixing

Finally, \mathcal{L}_{mix} describes the mixing between the $SU(2)_X$ and SM gauge groups [18, 67] via dimension-5 (dim-5) operators:

$$\mathcal{L}_{mix} = \sum_{i=1}^2 \frac{1}{\Lambda_i} \Delta_i^a X_a^{\mu\nu} Y_{\mu\nu} \sim \sum_{i=1}^2 \frac{\langle \Delta_i^a \rangle}{\Lambda_i} X_a^{\mu\nu} Y_{\mu\nu},\tag{2.9}$$

where the corresponding X^a mixes with the SM γ and Z once Δ_i^a obtains a VEV. In this work, we choose \mathcal{L}_{mix} to be

$$\mathcal{L}_{mix} = -\frac{\sin \chi}{2} X_3^{\mu\nu} Y_{\mu\nu} - \frac{\sin \chi'}{2} X_1^{\mu\nu} Y_{\mu\nu},\tag{2.10}$$

which implies X^1 and X^3 mixes with SM neutral gauge bosons at tree level. The reason why we include X^1 in the mixing is to enable the excited state ψ_2 to decay into the DM and a photon to explain the 3.5 keV X-ray line. Moreover, we assume $\sin \chi' \ll \sin \chi$ for simplicity and neglect the effect of $\sin \chi'$ in diagonalizing the gauge boson mass matrix.² The relevant

²It is a legitimate assumption as long as the lifetime of the excited state ψ_2 is less than 1 sec, thus having no influence on Big-Bang nucleosynthesis.

Lagrangian, with Lorentz indices suppressed, before and after diagonalizing the mass matrix of γ , Z and X^3 reads

$$\mathcal{L} \supset \begin{pmatrix} A_f & Z_f & X_f^3 \end{pmatrix} \begin{pmatrix} eJ_{EM} \\ gJ_Z \\ g_X J_X \end{pmatrix} = \begin{pmatrix} A_m & Z_m & X_m^3 \end{pmatrix} R \begin{pmatrix} eJ_{EM} \\ gJ_Z \\ g_X J_X \end{pmatrix}, \quad (2.11)$$

where e , g and g_X are $U(1)_{EM}$, $SU(2)_L$ and $SU(2)_X$ gauge couplings, respectively. The subscript f refers to the flavor states, m denotes the mass and kinetic eigenstates, and J s are currents.³ R is the rotation matrix connecting the flavor and mass basis of the gauge bosons [70]:

$$R = \begin{pmatrix} 1 & 0 & 0 \\ -\cos\theta_w \tan\chi \sin\zeta & \sin\theta_w \tan\chi \sin\zeta + \cos\zeta & \sec\chi \sin\zeta \\ -\cos\theta_w \tan\chi \cos\zeta & \sin\theta_w \tan\chi \cos\zeta - \sin\zeta & \sec\chi \cos\zeta \end{pmatrix}, \quad (2.12)$$

where

$$\begin{aligned} \tan(2\zeta) &= \frac{2\delta_X (m_{X^3}^2 - m_W^2 \sec^2\theta_w)}{(m_{X^3}^2 - m_W^2 \sec^2\theta_w)^2 - \delta_X^2}, \\ \delta_X &= -\frac{m_W^2 \sin\theta_w \tan\chi}{\cos^2\theta_w}. \end{aligned} \quad (2.13)$$

It is clear that $R = \mathbb{1}_{3 \times 3}$ if $\sin\chi = 0$. Note that the photon does not couple to J_X at tree-level but the interaction will be induced at loop-level. From now on, we will suppress the subscript m in the gauge bosons: A , Z and X_3 refer to the mass and kinetic eigenstates, unless otherwise stated.

3 Relevant annihilation cross-sections

In this section, we calculate the DM annihilation cross-sections into SM fermions and the excited state ψ_2 . The first process will give rise to γ -rays via fragmentation of quarks and final state radiation from leptons, while the second one will yield X-rays when ψ_2 decays back into the DM and a photon via $\sin\chi' X_1^{\mu\nu} Y_{\mu\nu}$ as shown in Fig. 1.

In this work, we focus on the regime, where $m_{X^a} > m_{DM}$, such that the GC gamma-ray excess and 3.5 keV X-ray line can be realized through DM annihilations into SM particles and excited χ_2 , respectively. As we shall see below, we need a large resonance enhancement in the annihilation cross-section coming from the X^3 narrow width; therefore, to a very good approximation, we only include X^3 -exchange processes in the computation.

³To be more precise, $J_{EM}^\mu = Q_f \bar{f} \gamma^\mu f$, while $J_Z = \frac{1}{\cos\theta_w} \bar{f} \gamma^\mu ((I_3 - \sin^2\theta_w Q_f) P_L + (-\sin^2\theta_w Q_f) P_R) f$ for a fermion f . $P_{L(R)}$ is the left- (right-)handed projection operator. J_X are defined in Eq. (2.5) and (2.8) for the Majorana and Dirac DM, respectively.

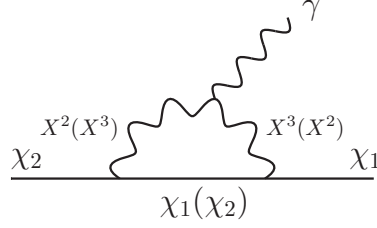


Figure 1: χ_2 decays into χ_1 and a photon through a dim-5 operator, $X_1^{\mu\nu}Y_{\mu\nu}$.

3.1 Majorana DM

For Majorana DM, we have the following relevant annihilation cross-sections: $\chi_1\chi_1 \rightarrow \bar{f}f$ (P -wave) for γ -ray and the DM density, $\chi_1\chi_1 \rightarrow \bar{\psi}_2\psi_2$ (P -wave), $\bar{\psi}_2\psi_2 \rightarrow \bar{f}f$ (S -wave) for the DM density. In order to account for the X-ray line, the mass splitting between m_{χ_1} and m_{ψ_2} is set to be 3.5 keV, which in turn implies that the S -wave $\bar{\psi}_2\psi_2 \rightarrow \bar{f}f$ is the dominant contribution to the DM abundance computation as opposed to the γ -ray excess and X-ray line, which arise from P -wave processes due to axial-vector interactions of χ_1 .

For χ_1 annihilating into SM fermions f of mass m_f via X_3 , as shown in Fig. 2, the relevant interactions are ⁴

$$\mathcal{L}_{\chi_1\chi_1 \rightarrow \bar{f}f} \supset -\frac{1}{2} (g_X \sec \chi \cos \zeta) X_\mu^3 \chi_1^\dagger \bar{\sigma}^\mu \chi_1 + X_\mu^3 \bar{f} \gamma^\mu (g_L P_L + g_R P_R) f, \quad (3.1)$$

where

$$\begin{aligned} g_L &= -eQ_f \cos \theta_w \tan \chi \cos \zeta + (\sin \theta_w \tan \chi \cos \zeta - \sin \zeta) \frac{g}{\cos \theta_w} (I_3 - \sin^2 \theta_w Q_f), \\ g_R &= -eQ_f \cos \theta_w \tan \chi \cos \zeta + (\sin \theta_w \tan \chi \cos \zeta - \sin \zeta) \frac{g}{\cos \theta_w} (-\sin^2 \theta_w Q_f), \end{aligned} \quad (3.2)$$

in which Q_f is the fermion electric charge and I_3 is the isospin, associated with left-handed field. The annihilation cross-section times the relative velocity v is,

$$(\sigma v)_{\chi_1\chi_1 \rightarrow \bar{f}f} = \sum_f \frac{(g_X \sec \chi \cos \zeta)^2 \sqrt{s - 4m_f^2}}{48\pi m_{X_3}^4 s^{3/2} \left((s - m_{X_3}^2)^2 + \Gamma_{X_3}^2 m_{X_3}^2 \right)} (\lambda_{\sigma_1} + \lambda_{\sigma_2} - \lambda_{\sigma_3}), \quad (3.3)$$

⁴Again, we use the Weyl spinor notation for Majorana χ_1 .

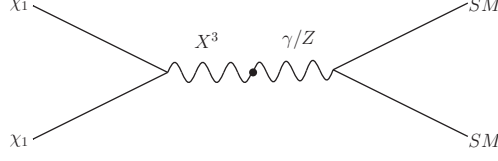


Figure 2: $\chi_1\chi_1$ annihilate into SM particles that fragment into photons, which are responsible for GC gamma rays.

where

$$\begin{aligned}
s &= \frac{4m_{\chi_1}^2}{1 - v^2/4}, \\
\lambda_{\sigma_1} &= s^2 \left(m_{X^3}^4 (g_L^2 + g_R^2) + 6m_{\chi_1}^2 m_f^2 (g_L - g_R)^2 \right), \\
\lambda_{\sigma_2} &= 2m_{X^3}^4 m_{\chi_1}^2 m_f^2 (5g_L^2 - 18g_L g_R + 5g_R^2), \\
\lambda_{\sigma_3} &= s m_{X^3}^2 \left(4m_{\chi_1}^2 (m_{X^3}^2 (g_L^2 + g_R^2) + 3m_f^2 (g_L - g_R)^2) + m_{X^3}^2 m_f^2 (g_L^2 - 6g_L g_R + g_R^2) \right).
\end{aligned}$$

Note that one has to sum over all different final states as denoted by \sum_f . To simplify the expression, we employ the resonant limit of $m_{\chi_1} = \frac{1}{2}m_{X^3}$ on the matrix element while keeping the kinetic part intact.⁵ The annihilation cross-section reads, up to the second order in v^2 ,

$$(\sigma v)_{\chi_1\chi_1 \rightarrow \bar{f}f} \simeq \sum_f \frac{(g_X \sec \chi \cos \zeta)^2 \sqrt{s - 4m_f^2}}{96\pi \left((s - m_{X^3}^2)^2 + \Gamma_{X^3}^2 m_{X^3}^2 \right)} m_{\chi_1} (g_1 v^2 + g_2 v^4), \quad (3.4)$$

with

$$\begin{aligned}
g_1 &= (g_L^2 + g_R^2) - \frac{m_f^2 (g_L^2 - 6g_L g_R + g_R^2)}{4m_{\chi_1}^2}, \\
g_2 &= \frac{1}{8} \left((g_L^2 + g_R^2) + \frac{m_f^2 (g_L^2 - 3g_L g_R + g_R^2)}{m_{\chi_1}^2} \right).
\end{aligned}$$

Similarly, for $\bar{\psi}_2\psi_2 \rightarrow \bar{f}f$, which is relevant for the relic abundance computation, we have, up to the first order in v^2 ,

$$(\sigma v)_{\bar{\psi}_2\psi_2 \rightarrow \bar{f}f} \simeq \sum_f \frac{(g_X \sec \chi \cos \zeta)^2 \sqrt{s - 4m_f^2}}{64\pi \left((s - m_{X^3}^2)^2 + \Gamma_{X^3}^2 m_{X^3}^2 \right)} m_{\psi_2} (h_1 + h_2 v^2), \quad (3.5)$$

⁵We apply this simplification to annihilation cross-sections below as well.

with

$$\begin{aligned}
s &= \frac{4m_{\psi_2}^2}{1 - v^2/4}, \\
h_1 &= (g_L^2 + g_R^2) - \frac{m_f^2 (g_L^2 - 6g_L g_R + g_R^2)}{4m_{\psi_2}^2}, \\
h_2 &= \frac{5}{24} (g_L^2 + g_R^2) + \frac{m_f^2 (g_L^2 - 6g_L g_R + g_R^2)}{96m_{\psi_2}^2}.
\end{aligned}$$

In addition, the X^3 decay width Γ_{X^3} is given by, including the channels into χ_1 , ψ_2 and SM fermions,

$$\Gamma_{X^3} = \Gamma_{X^3 \rightarrow \chi_1 \chi_1} + \Gamma_{X^3 \rightarrow \bar{\psi}_2 \psi_2} + \sum_f \Gamma_{X^3 \rightarrow \bar{f} f}, \quad (3.6)$$

where

$$\begin{aligned}
\Gamma_{X^3 \rightarrow \chi_1 \chi_1} &= \Theta(m_{X^3} - 2m_{\chi_1}) (g_X \sec \chi \cos \zeta)^2 \frac{(m_{X^3}^2 - 4m_{\chi_1}^2)^{3/2}}{96\pi m_{X^3}^2}, \\
\Gamma_{X^3 \rightarrow \bar{\psi}_2 \psi_2} &= \Theta(m_{X^3} - 2m_{\psi_2}) (g_X \sec \chi \cos \zeta)^2 \frac{(m_{X^3}^2 - m_{\psi_2}^2) (m_{X^3}^2 - 4m_{\psi_2}^2)^{1/2}}{96\pi m_{X^3}^2}, \\
\Gamma_{X^3 \rightarrow \bar{f} f} &= \Theta(m_{X^3} - 2m_f) \sqrt{m_{X^3}^2 - 4m_f^2} \frac{m_{X^3}^2 (g_L^2 + g_R^2) - m_f^2 (g_L^2 - 6g_L g_R + g_R^2)}{24\pi m_{X^3}^2}.
\end{aligned} \quad (3.7)$$

On the other hand, $\chi_1 \chi_1 \rightarrow \bar{\psi}_2 \psi_2$ with subsequent decay of ψ_2 (or $\bar{\psi}_2$) into χ_1 and γ explaining the 3.5 keV X-ray line, as shown in Fig. 3, has the cross-section

$$(\sigma v)_{\chi_1 \chi_1 \rightarrow \bar{\psi}_2 \psi_2} = \frac{(g_X \sec \chi \cos \zeta)^4 \sqrt{s - 4m_{\psi_2}^2}}{192\pi m_{X^3}^4 s^{3/2} \left((s - m_{X^3}^2)^2 + \Gamma_{X^3}^2 m_{X^3}^2 \right)} (\kappa_{\sigma_1} + \kappa_{\sigma_2}), \quad (3.8)$$

where

$$\begin{aligned}
\kappa_{\sigma_1} &= 6s^2 m_{\chi_1}^2 m_{\psi_2}^2 - 12s m_{X^3}^2 m_{\chi_1}^2 m_{\psi_2}^2, \\
\kappa_{\sigma_2} &= m_{X^3}^4 (2m_{\chi_1}^2 (5m_{\psi_2}^2 - 2s) + s(s - m_{\psi_2}^2)).
\end{aligned} \quad (3.9)$$

For $m_{\chi_1} \simeq m_{\psi_2}$, we have to a very good approximation, up to the second order in v^2 :

$$(\sigma v)_{\chi_1 \chi_1 \rightarrow \bar{\psi}_2 \psi_2} \simeq \frac{(g_X \sec \chi \cos \zeta)^4 \sqrt{s - 4m_{\psi_2}^2}}{1536\pi \left((s - m_{X^3}^2)^2 + \Gamma_{X^3}^2 m_{X^3}^2 \right)} m_{\chi_1} (v^2 (3 + v^2)). \quad (3.10)$$

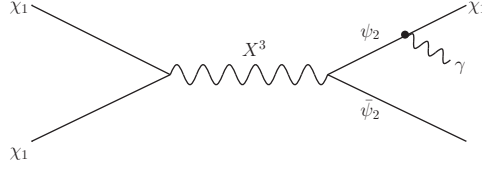


Figure 3: $\chi_1\chi_1$ annihilation into $\bar{\psi}_2\psi_2$ responsible for the X-ray line.

3.2 Dirac DM

For Dirac DM, the distinctive feature compared to the Majorana case is that all relevant processes are S -wave dominated due to the vector interactions of ψ_1 . The annihilation cross-section of $\bar{\psi}_1\psi_1 \rightarrow \bar{f}f$ is, up to the first order in v^2 ,

$$(\sigma v)_{\bar{\psi}_1\psi_1 \rightarrow \bar{f}f} \simeq \sum_f \frac{(g_X \sec \chi \cos \zeta)^2 \sqrt{s - 4m_f^2}}{64\pi \left((s - m_{X^3}^2)^2 + \Gamma_{X^3}^2 m_{X^3}^2 \right)} m_{\psi_1} (\omega_1 + \omega_2 v^2), \quad (3.11)$$

with

$$\begin{aligned} s &= \frac{4m_{\psi_1}^2}{1 - v^2/4}, \\ \omega_1 &= (g_L^2 + g_R^2) - \frac{m_f^2 (g_L^2 - 6g_L g_R + g_R^2)}{4m_{\psi_1}^2}, \\ \omega_2 &= \frac{5}{24} (g_L^2 + g_R^2) + \frac{m_f^2 (g_L^2 - 6g_L g_R + g_R^2)}{96m_{\psi_1}^2}. \end{aligned}$$

and for $\bar{\psi}_1\psi_1 \rightarrow \bar{\psi}_2\psi_2$ we have

$$(\sigma v)_{\bar{\psi}_1\psi_1 \rightarrow \bar{\psi}_2\psi_2} \simeq \frac{(g_X \sec \chi \cos \zeta)^4 \sqrt{s - 4m_{\psi_2}^2}}{393216\pi \left((s - m_{X^3}^2)^2 + \Gamma_{X^3}^2 m_{X^3}^2 \right)} m_{\psi_1} (1152 + 336v^2 + 83v^4). \quad (3.12)$$

Note that the X^3 partial decay width into $\bar{\psi}_1\psi_1$ becomes

$$\Gamma_{X^3 \rightarrow \bar{\psi}_1\psi_1} = \Theta(m_{X^3} - 2m_{\psi_1}) (g_X \sec \chi \cos \zeta)^2 \frac{(m_{X^3}^2 - m_{\psi_1}^2) (m_{X^3}^2 - 4m_{\psi_1}^2)^{1/2}}{96\pi m_{X^3}^2} \quad (3.13)$$

Furthermore, the Dirac DM ψ_1 will have sizable DM-nucleon interactions in the context of direct detections. The effective DM-quark interaction reads,

$$\mathcal{L} \supset -\frac{(g_X \sec \chi \cos \zeta) (g_L + g_R)}{8m_{X^3}^4} \bar{\psi}_1 \gamma^\mu \psi_1 \bar{f} \gamma_\mu f, \quad (3.14)$$

where g_L and g_R are defined in Eq. 3.2.

4 Observables

Based on the DM annihilation cross-sections into the excited state and SM fermions, we now describe how to compute the flux of X-rays and γ -rays, and will comment on the DM relic density computation.

4.1 X-ray

Recently, a potential signal of a monochromatic photon line from the Perseus cluster at energy around 3.56 keV has been identified from the XMM-Newton data [16, 17]. The flux of such a monochromatic photon line at the X-ray energy $E_\gamma = 3.56$ keV is measured to be $\Phi_{\gamma\gamma} = 5.2^{+3.70}_{-2.13} \times 10^{-5}$ ph cm $^{-2}$ s $^{-1}$ [17]. Although the source of this X-ray line signal is still unclear, the DM annihilation (or decay) into photons is a well motivated possibility [18–36, 38–65]. Considering the Perseus Mass $\simeq 1.49 \times 10^{14} M_\odot$ and the distance between the Perseus cluster and the solar system $\simeq 78$ Mpc, the photon-line flux from DM annihilation can be written as

$$\frac{\Phi_{\gamma\gamma}}{\text{cm}^{-2}\text{s}^{-1}} = 2.08 \times 10^{-3} \times \left[\frac{1 \text{ GeV}}{m_{\text{DM}}} \right]^2 \times \frac{\mathcal{D} \langle \sigma v \rangle_{\gamma\gamma}}{10^{-19} \text{cm}^3 \text{s}^{-1}}, \quad (4.1)$$

where \mathcal{D} is 1 for Majorana DM and 1/2 for Dirac DM. The monochromatic annihilation cross section $\langle \sigma v \rangle_{\gamma\gamma}$ is the relative velocity averaged with all the DM inside the Perseus cluster. Here, we adopt the relative velocity $v_{\text{rel.}}$ described by the Maxwell-Boltzmann distribution [71],

$$f(v_{\text{rel.}}) = \frac{v_{\text{rel.}}^2}{2\sqrt{\pi}v_0^3} \exp \left[\frac{-v_{\text{rel.}}^2}{4v_0^2} \right], \quad (4.2)$$

where we take the mean value of the velocity dispersion $v_0 \sim 10^{-3} c$ [71]. One can see that a DM mass $m_{\text{DM}} \sim 10$ GeV requires $\langle \sigma v \rangle_{\gamma\gamma} \sim 2.5 \times 10^{-19} \text{cm}^3 \text{s}^{-1}$ in order to explain the X-ray signal from the Perseus cluster.

It is worthy to mention that the information of Perseus mass, which is constrained by the velocity dispersion, can substantially reduce the uncertainties arising from halo inner slope. In Ref. [39], an overall uncertainty about a factor of 5 was obtained for the DM flux predicted in Eq. (4.1).

4.2 GC γ -ray

A gamma-ray excess in the GC region, found in the Fermi-LAT data, has been widely studied in the context of DM annihilation [2–7, 10–12]. Assuming spherical symmetry, the spatial distribution of such an excess can be explained by DM annihilation in the generalized Navarro-Frenk-White (gNFW, [72, 73]) profile,

$$\rho(r) = \rho_s \frac{(r/r_s)^{-\gamma}}{(1 + r/r_s)^{3-\gamma}}. \quad (4.3)$$

To explain the gamma-ray excess, the inner slope γ parameter requires $\gamma = 1.2$ [11, 74]. In this work, we adopt this value together with the local density $\rho(8.5 \text{ kpc}) = 0.4 \text{ GeV/cm}^3$ and $r_s = 20 \text{ kpc}$.

The differential diffuse gamma-ray flux along a line-of-sight (l.o.s.) at an open angle relative to the direction of the GC is given by

$$\frac{dN}{dE} = \frac{\langle \sigma v \rangle_\gamma}{\mathcal{D} \pi m_\chi^2} \frac{dN_\gamma}{dE} \int_{\text{l.o.s.}} ds \rho^2(r(s, \psi)), \quad (4.4)$$

where \mathcal{D} is 8 for Majorana DM but 16 for Dirac one. The $\langle \sigma v \rangle_\gamma$ is the velocity averaged annihilation cross section at the GC. However, the mean value of the velocity dispersion v_0 in Eq. (4.2) is $\sim 10^{-4} c$ at the GC region [71, 75].

The $\frac{dN_\gamma}{dE}$ is the photon energy distribution per annihilation. All possible annihilation channels are included. The branching ratio of all the possible annihilation channels can be obtained by using Eq. (3.4) and (3.11). For each annihilation channel, the corresponding $\frac{dN_\gamma}{dE}$ is taken from the numerical PPPC4 table [76].

One has to bear in mind that the background uncertainties for the GC gamma ray excess can significantly change the DM parameter space. Therefore, in order to include the background uncertainties, we use the central values and error bars in Fig. 17 from Ref. [77], where the systematic uncertainties coming from the Galactic diffuse emission have been properly included. Following Ref. [77], the inner Galactic central region described by the Galactic longitude l and latitude b is

$$|\ell| \leq 20^\circ \quad \text{and} \quad 2^\circ \leq |b| \leq 20^\circ. \quad (4.5)$$

We conclude this section with Fig. 4 where the data on γ -ray spectrum is taken from Ref. [77] and the photon spectra are calculated using our best-fit points in both the Majorana (solid red line) and Dirac cases (dashed blue line), for which we include the γ -ray and X-ray data into fitting. One can see the GC γ -ray excess, a distinctive bump around a few GeV, can be well explained by DM annihilations into the SM fermions, which then fragment into photons. The continuous photon spectrum mainly comes from the decay of neutral pions, which are originated from the fragmentation of the quarks in the annihilation of the dark matter. In addition, the quarks can also fragment into charged pions, which subsequently decay into muons and eventually electrons. The dark matter can also directly annihilate into taus, muons, and electrons. The taus and muons will eventually decay into electrons. Although all these electrons undergo the inverse Compton scattering and bremsstrahlung, which can only give rise to photons at the lower photon energy, it does not effect the region of $E_\gamma > 1 \text{ GeV}$ [78]. As a result, we do not consider inverse Compton scattering and bremsstrahlung in this study.

4.3 DM relic abundance

The DM relic density can be obtained by solving the Boltzmann equation for the DM density evolution with the thermally-averaged annihilation cross-section into SM fermions. In

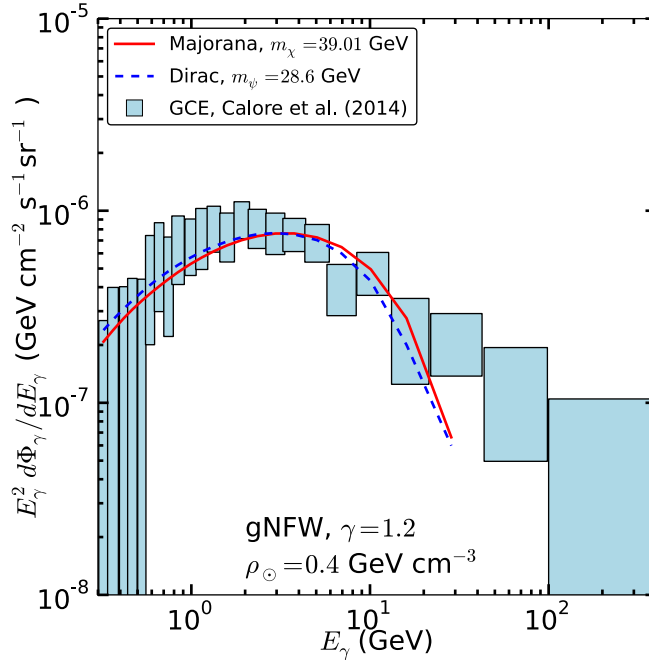


Figure 4: *GC γ -ray excess spectrum taken from Ref. [77]. We also show the corresponding photon spectra obtained for the Majorana (solid red line) and Dirac (dashed blue line) case.*

this work, we assume that the thermal relic scenario such that the current relic density is determined by the DM annihilation and coannihilation of the excited state, and the number densities of these particles follow the Boltzmann distribution before freeze-out. Note that, in the context of the relic density calculation, one cannot simply assume $v \ll 1$, that is only valid in the X -ray and γ -ray flux computation. Instead, one has to properly take into account the thermal average effect. Following Ref. [79], we compute the thermal relic density from the thermally averaged annihilation cross-section based on Eqs. (3.3), (3.5) and (3.11). However, the effective relativistic degrees of freedom are taken from the default numerical table of DarkSUSY [80]. Also, we use the PLANCK result of $\Omega h^2 = 0.120$ [81] together with the 10% theoretical error to constrain the relic density.

A comment on the DM density computation is in order here. Due to a small mass splitting of 3.5 keV between the DM particle and excited state to account for the X -ray line, coannihilation processes involving the excited state have to be taken into account. As mentioned above, we focus on the scenario with the resonance enhancement via the X^3 exchange. As a result, the only relevant interactions are the DM annihilation and excited state annihilation into SM fermions. For the Majorana DM case, the dominant contribution to relic abundance comes from the excited state annihilation, $\psi_2 \bar{\psi}_2 \rightarrow \bar{f} f$, which is dominated by S -wave due to the Dirac nature of ψ_2 , while $\chi_1 \chi_1 \rightarrow \bar{f} f$ is P -wave suppressed because of χ_1 being Majorana. Furthermore, the large resonance enhancement in the process $\chi_1 \chi_1 \rightarrow \bar{f} f$ required to explain the X -ray line at current time ($v \sim 10^{-3}c$) is no longer the case at the

time of freeze-out, because during the freeze-out the relative velocity is much larger of order $\sim \frac{1}{3}c$ such that the annihilation deviates considerably away from the resonance region. Therefore, $\langle\sigma v\rangle(\chi_1\chi_1 \rightarrow \bar{f}f)$ at freeze-out is much smaller than the current annihilation cross-section $10^{-26} \text{ cm}^3\text{sec}^{-1}$, which is the right size to accommodate the GC γ -ray excess.⁶ Hence, $\chi_1\chi_1 \rightarrow \bar{f}f$ alone cannot give rise to the correct relic density, which roughly requires an annihilation cross section of $3 \times 10^{-26} \text{ cm}^3\text{sec}^{-1}$. For the Majorana DM case, this problem can be circumvented by the S -wave process $\psi_2\bar{\psi}_2 \rightarrow \bar{f}f$, which can give an annihilation cross section of order $10^{-26} \text{ cm}^3\text{sec}^{-1}$ to explain the relic abundance.

In the Dirac DM case, however, both ψ_1 and ψ_2 are Dirac particles and all processes are S -wave dominated. In the context of the DM density, annihilations of ψ_1 and those of ψ_2 contribute almost equally due to the nearly degenerate mass spectrum. However, the annihilation cross sections of both processes are much smaller than $10^{-26} \text{ cm}^3\text{sec}^{-1}$ at freeze-out due to the deviation from the resonance region as explained above. Therefore, one has to involve an additional DM annihilation mechanism to reduce the relic abundance. A possible solution, for instance, is to embed $(\chi_2, \chi_1)^T$ into a larger multiplet such as $(\chi_4, \chi_2, \chi_1, \chi_3)^T$ such that coannihilations between χ_1 and χ_3 via $X^{1,2}$ is possible to bring down the relic density. As long as the mass difference between m_{χ_3} and m_{χ_1} is much larger than 3.5 keV, χ_3 cannot be generated currently and thus the existence of χ_3 is irrelevant to the X-ray line and γ -ray excess.

We summarize the discussion here with Table 3, where we show the cross-sections in orders of magnitude at the time of freeze-out and the current time. It is clear that only Majorana DM can accommodate the correct relic density due to the dominant contribution from the S -wave process $\bar{\psi}_2\psi_2 \rightarrow \bar{f}f$.

| Majorana DM | $\langle\sigma v\rangle_{\chi_1\chi_1 \rightarrow \bar{f}f}$ | $\langle\sigma v\rangle_{\bar{\psi}_2\psi_2 \rightarrow \bar{f}f}$ | $\langle\sigma v\rangle_{\chi_1\chi_1 \rightarrow \bar{\psi}_2\psi_2}$ |
|-------------|--|--|--|
| freeze-out | 10^{-31} | 10^{-26} | 10^{-24} |
| current | 10^{-26} (GC γ -ray) | 0 | 10^{-19} (X-ray) |
| Dirac DM | $\langle\sigma v\rangle_{\bar{\psi}_1\psi_1 \rightarrow \bar{f}f}$ | $\langle\sigma v\rangle_{\bar{\psi}_2\psi_2 \rightarrow \bar{f}f}$ | $\langle\sigma v\rangle_{\bar{\psi}_1\psi_1 \rightarrow \bar{\psi}_2\psi_2}$ |
| freeze-out | 10^{-31} | 10^{-31} | 10^{-24} |
| current | 10^{-26} (GC γ -ray) | 0 | 10^{-19} (X-ray) |

Table 3: *Relevant cross-sections in orders of magnitude in units of $\text{cm}^{-3}\text{sec}^{-1}$ at the freeze-out and at the current time. $\langle\sigma v\rangle_{\chi_1\chi_1 \rightarrow \bar{\psi}_2\psi_2}$ and $\langle\sigma v\rangle_{\bar{\psi}_1\psi_1 \rightarrow \bar{\psi}_2\psi_2}$ at freeze-out are not relevant for DM relic density computation.*

⁶One might think that S -wave dominated interactions will have the same cross-section at freeze-out as the current one while P -wave dominated ones have the larger cross-section at freeze-out due to the larger DM velocity ($\sim \frac{1}{3}c$) compared to the current velocity ($\sim 10^{-3}c$). However, it is not always true, especially when the resonance enhancement takes place as we shall see later.

5 Results

In order to employ the resonance enhancement, we rewrite $m_{X^3} = (2 - \delta)m_{DM}$ with $m_{DM} = m_{\chi_1}$ (m_{ψ_1}) in the Majorana (Dirac) DM case. Therefore, at phenomenological level we choose m_{χ_1} , g_X , δ and $\sin \chi$ as 4 independent input parameters to investigate if the proposed non-abelian DM models can simultaneously account for the GC γ -ray excess and the 3.5 keV X-ray line, and thermally reproduce the correct relic abundance.

Before moving into the numerical analysis, we would like to comment on the region of interest for $\sin \chi$. For illustration, we choose the Majorana DM case but the Dirac DM case exhibits the same feature. As mentioned above, we aim for $\langle \sigma v \rangle_{\chi_1 \chi_1 \rightarrow \bar{\psi}_2 \psi_2} \sim 10^{-19} \text{ cm}^3 \text{ sec}^{-1}$ to explain the 3.5 keV X-ray line and $\langle \sigma v \rangle_{\chi_1 \chi_1 \rightarrow \bar{f} f} \sim 10^{-26} \text{ cm}^3 \text{ sec}^{-1}$ to realize the GC γ -ray excess. On the other hand, we have from Eq. (3.4) and (3.10) in the limit of $m_{X^3} \simeq 2m_{\chi_1}$, $v \ll 1$ and $m_f \simeq 0$,

$$\begin{aligned} (\sigma v)_{\chi_1 \chi_1 \rightarrow \bar{f} f} &\sim \frac{\sqrt{s}}{\left((s - m_{X^3}^2)^2 + \Gamma_{X^3}^2 m_{X^3}^2\right)} (g_L^2 + g_R^2) v^2 \sim \frac{\sqrt{s}}{m^4 v_{\text{rel}}^4 + 4m_{\chi_1}^2 \Gamma_{X^3}^2} \sin^2 \chi v^2, \\ (\sigma v)_{\chi_1 \chi_1 \rightarrow \bar{\psi}_2 \psi_2} &\sim \frac{\sqrt{s - 4m_{\psi_2}^2}}{\left((s - m_{X^3}^2)^2 + \Gamma_{X^3}^2 m_{X^3}^2\right)} v^2 \sim \frac{\sqrt{s - 4m_{\psi_2}^2}}{m^4 v_{\text{rel}}^4 + 4m_{\chi_1}^2 \Gamma_{X^3}^2} v^2, \end{aligned} \quad (5.1)$$

where we have suppressed the kinematics factors and the coupling constant g_X , which do not affect the argument. It is clear that in order to achieve $\langle \sigma v \rangle_{\text{X-ray}} / \langle \sigma v \rangle_{\gamma} \sim 10^7$, one must have $\sin^2 \chi$ smaller than 10^{-7} . It implies that in the denominator of the cross-section, $\Gamma_{X^3}^2 m_{X^3}^2 \sim \left(\frac{1}{16\pi^2}\right)^2 m_{\chi_1}^4 \sin^4 \chi$ becomes negligible compared to $m_{\chi_1}^4 v^4$ with $v \sim 10^{-3} c$. In other words, we saturate the resonance enhancement since the DM velocity becomes dominant in the denominator and any further decrease in $\sin \chi$ will not affect the cross-section. In Fig. 5, we can clearly see that for both the Majorana and Dirac case, $\sin \chi$ is located in the saturated area, i.e., $\sin \chi \ll v$. Furthermore, the reasons why the required mixing is so small, $\sin^2 \chi \ll 10^{-7}$, are because first, $\langle \sigma v \rangle_{\chi_1 \chi_1 \rightarrow \bar{\psi}_2 \psi_2}$ has a large kinematical suppression factor, $\sqrt{s - 4m_{\psi_2}^2}$, compared to $\langle \sigma v \rangle_{\chi_1 \chi_1 \rightarrow \bar{f} f}$ and second, the v for X-rays in the Perseus cluster is larger than the v for γ -rays in the GC. Subsequently, $\langle \sigma v \rangle_{\chi_1 \chi_1 \rightarrow \bar{\psi}_2 \psi_2}$ is much smaller than $\langle \sigma v \rangle_{\chi_1 \chi_1 \rightarrow \bar{f} f}$ with $\sin \chi \sim 1$. It indicates that one actually needs $\sin^2 \chi \ll 10^{-7}$ in order to fulfill $\langle \sigma v \rangle_{\text{X-ray}} / \langle \sigma v \rangle_{\gamma} \sim 10^7$.

For the fitting procedure, we make use of the minimum chi-squared method. Since the likelihoods for the relic density, X-ray line, and GC γ -rays data are well Gaussian-distributed, and the 95% and 99.73% confidence limits in two-dimensional contour plots correspond to $\delta\chi^2 = 5.99$ and $\delta\chi^2 = 11.83$, respectively.

5.1 Majorana case

In this section, we present the results in the Majorana DM case with the Majorana DM χ_1 and the Dirac excited state ψ_2 . Throughout this (and also next) section, the way we present

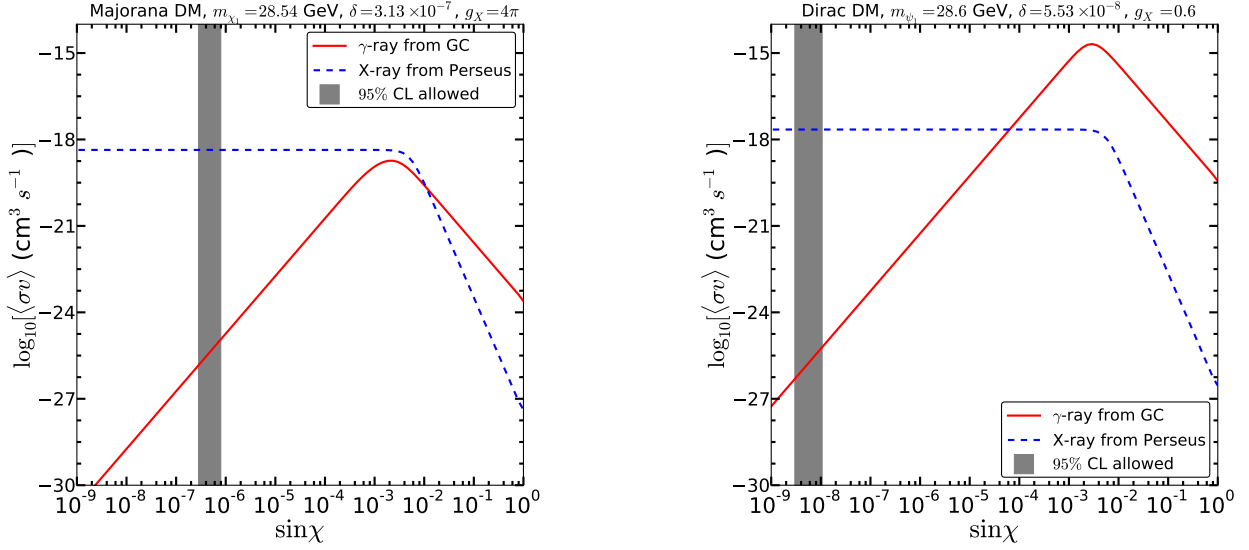


Figure 5: *Left panel: the Majorana case. Right panel: the Dirac case. The grey band represents the 95% confidence region for the γ -rays and X-rays data.*

the results is to project confidence regions into planes of parameters or observables.⁷ In the figures, inside the legend: “GC+Perseus” means that the confidence regions are obtained from the fit with only the GC γ -ray and X-ray data, while “GC+Perseus+ Ωh^2 ” indicates that the DM relic density is also included in the fitting in addition to the γ - and X-ray data.

In Fig. 6, we show the confidence regions in terms of the DM annihilation cross-section for the X-ray and γ -ray versus the DM mass. In the upper panels, we include the GC γ -ray excess and X-ray line only while the DM density is also included in the lower panels. The green (blue) area corresponds to the 95% (99.73%) confidence region while the red star represents the best-fit point. Furthermore, the unitarity bound [82] denoted by the red line comes from

$$\langle\sigma v\rangle \lesssim \frac{3 \times 10^{-22} \text{ cm}^3/\text{sec}}{m_{\chi_1}/(1 \text{ TeV})}. \quad (5.2)$$

We would like to make the following comments.

- The corresponding X-ray cross-section (left panels) is centered around $10^{-18} \text{ cm}^3/\text{sec}$ consistent with Eq. (4.1) while for γ -rays (right panels), one needs $\langle\sigma v\rangle \sim 10^{-26} \text{ cm}^3/\text{sec}$ complying with Ref. [77].
- The γ -ray spectrum coming from $\chi_1\chi_1 \rightarrow \bar{f}f$ certainly depends on the final states. In this model, the final states include both quarks and leptons, and the final state composition is fixed according to Eq. (3.1) and (3.2). In general, a quark final state demands a higher DM mass due to soft photon spectra compared to a leptonic one.

⁷In Fig. 6, for instance, we project the confidence region into the $\langle\sigma v\rangle_{\text{X-ray}}-m_{\chi_1}$ (left panels) and $\langle\sigma v\rangle_{\gamma}-m_{\chi_1}$ (right panels) plane.

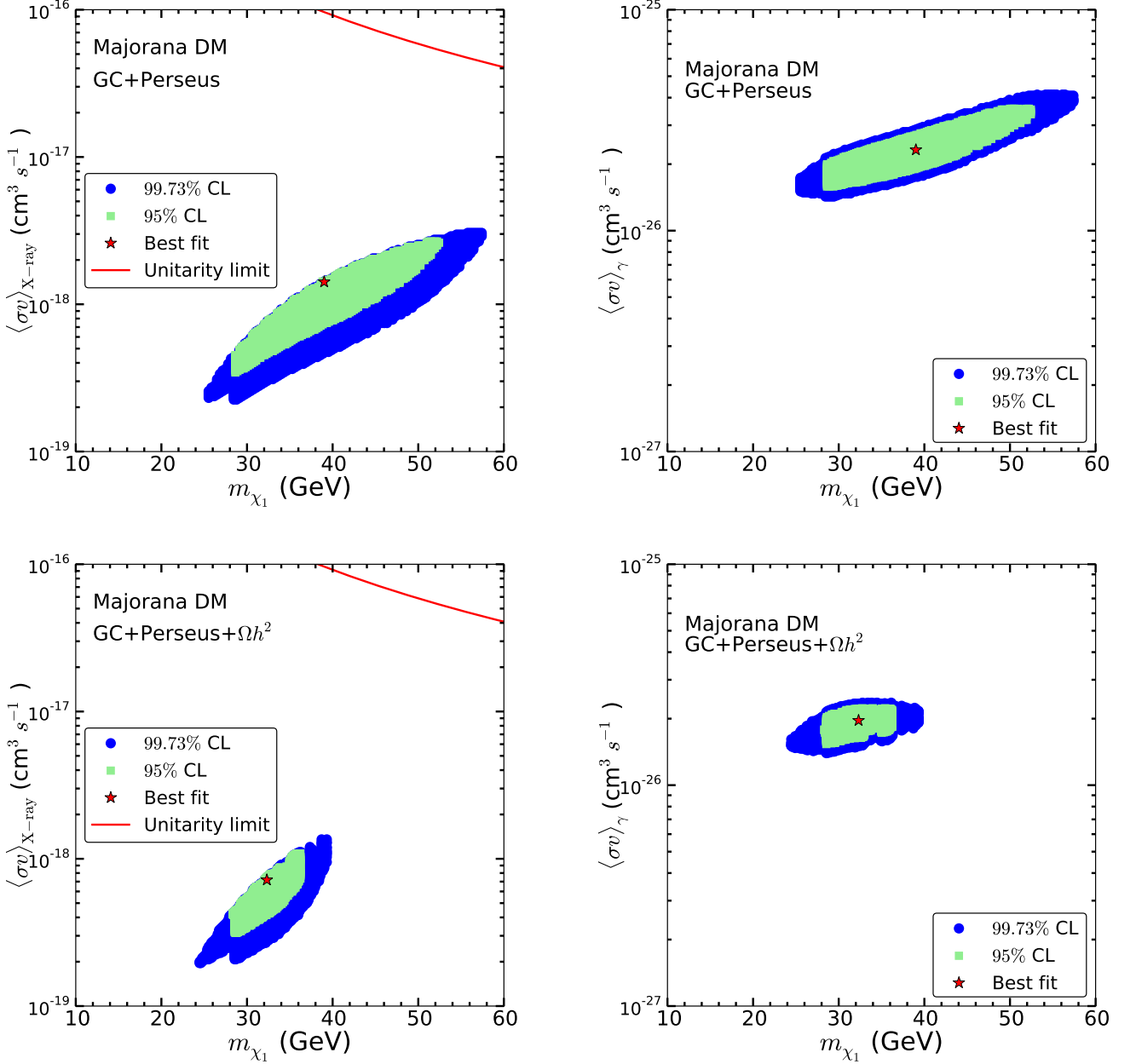


Figure 6: The 95% and 99.73% confidence-level regions in the plane of annihilation cross sections versus the DM mass obtained in the fits with (i) GC gamma-ray and Perseus X-ray data (upper panels) and (ii) also the DM relic density (lower panels) for the Majorana DM case. We show on the left panels: $\langle\sigma v\rangle_{X\text{-ray}}$ versus m_{χ_1} for X-rays, and on the right panels: $\langle\sigma v\rangle_{\gamma}$ versus m_{χ_1} for γ -rays.

Therefore, m_{χ_1} will lie between that of the purely b -quark case and that of purely τ case.

- For X-ray plots (left panels), there exists a sharp cut-off close to the best-fit point on

the top of the confidence regions. It is due to the perturbative limit: $g_X \leq 4\pi$ as we shall see later the best-fit point has g_X quite close to 4π . In contrast, the best-fit points for γ -ray plots (right panels) are located near the central area of the confidence region, which comes from the fact the $\langle\sigma v\rangle_\gamma$ can be enlarged by increasing the mixing $\sin\chi$ between the SM and dark sector without varying g_X as shown in Fig. 5 while $\langle\sigma v\rangle_{\text{X-ray}}$ is insensitive to $\sin\chi$ in the saturated area.

- All plots exhibit a sharp cut-off on 2σ regions especially on the left-hand side. It is due to the fact that GC γ -ray bump shown in Fig. 4 has a sharp drop around 0.5 GeV compared to the milder change on the right hand side around 20 GeV. Consequently, the bump of the predicted photon spectrum will not coincide with that of the GC excess, leading to a surge in chi-square, once m_{χ_1} becomes much smaller than the best-fit value.
- As explained in Section 4.3, the Majorana DM case can accommodate the correct DM density with the S -wave process $\psi_2\psi_2 \rightarrow \bar{f}f$ being the main contribution. Including the DM relic constraint reduces the confidence region significantly; only in the region of $25 \lesssim m_{\chi_1} \lesssim 40$ GeV can the model yield the correct DM density.

In Fig. 7, we show g_X versus m_{χ_1} in the upper panels and $\sin\chi$ versus m_{χ_1} in the lower panels. For the left panels, only the γ -ray and X-ray data are included in the fits while the DM density is also included in the right panels. Note that both $\chi_1\chi_1 \rightarrow \bar{f}f$ responsible for the GC γ -ray excess and $\chi_1\chi_1 \rightarrow \bar{\psi}_2\psi_2$ for the X-ray line are P-wave suppressed by the small DM velocity in the current Universe. To compensate for the velocity suppression, one needs large g_X in addition to the resonance enhancement to realize the very large $\langle\sigma v\rangle$, which is proportional to g_X^4 , for the X-ray line. It turns out that g_X is close to the perturbativity limit 4π for the best-fit point. In contrast, as we shall see later, the Dirac case features S -wave dominated cross-sections, i.e., without the velocity suppression, where g_X can be much smaller (~ 1). The mixing between the SM and the dark sector is roughly of order 10^{-7} but with a dip for $m_{\chi_1} = \frac{1}{2}m_Z$. It comes from large ζ defined in Eq. (2.13) for $m_{X^3} (= 2m_{\chi_1}) \simeq m_Z$, leading to large $g_{L,R}$ ($\sim \sin\zeta$) defined in Eq. (3.2) and large $\langle\sigma v\rangle_\gamma$. On the other hand, $\langle\sigma v\rangle_{\text{X-ray}}$ ($\sim \cos\zeta$) does not change dramatically for $m_{\chi_1} = \frac{1}{2}m_Z$. So as to maintain $\langle\sigma v\rangle_{\text{X-ray}}/\langle\sigma v\rangle_\gamma \sim 10^7$, smaller $\sin\chi$ is needed to suppress the γ -ray flux with respect to the X-ray one. Note that when $m_{X^3} \sim m_Z$, the electroweak precision data put a stringent bound on the SM-dark sector mixing, $\sin\chi \lesssim 5 \times 10^{-3}$ [83], which is however too weak to constrain any relevant parameter space of the model under consideration.

We conclude this section with Fig. 8, in which we project the confidence regions, including the X-ray and γ -ray data only, into the DM relic density and m_{χ_1} plane. It is clear that only for $25 \leq m_{\chi_1} \leq 40$ GeV, the correct DM density can be reproduced. Furthermore, the best-fit point corresponds to the slightly lower relic density, which results in a minor shift in the best-fit point when the DM relic density is included into the fit, as can be seen from Fig. 6 and 7.

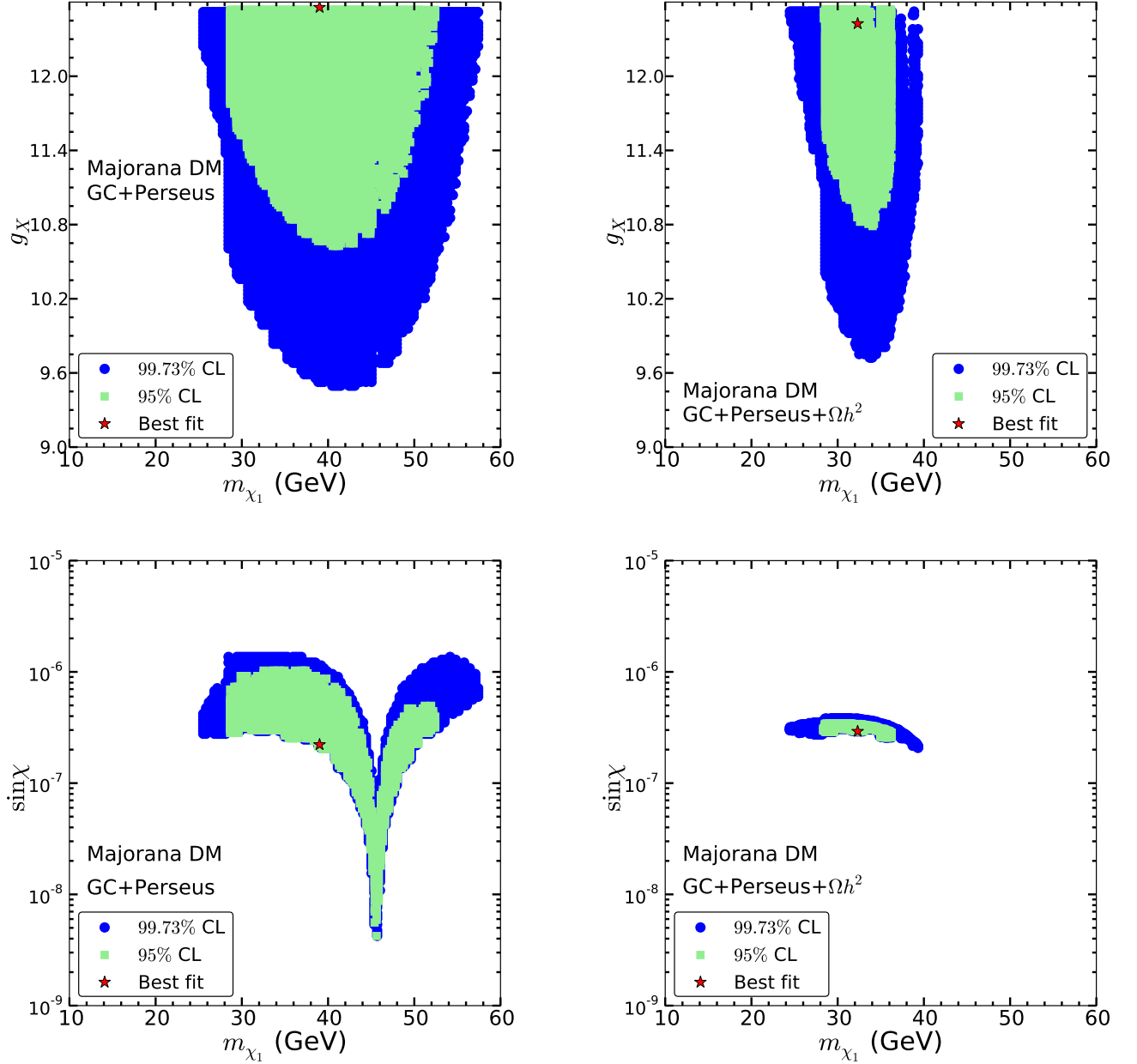


Figure 7: The 95% and 99.73% confidence-level regions in the planes of (m_{χ_1}, g_X) (upper panels) and $(m_{\chi_1}, \sin \chi)$ (lower panels) obtained in the fits with (i) GC gamma-ray and Perseus X-ray data (left panels) and (ii) also the DM relic density (right panels) for the Majorana DM case.

5.2 Dirac case

Here we show the results of the Dirac DM case. As argued in Sec. 4.3, all relevant processes responsible for the X-ray line, GC γ -ray excess and DM relic density are S -wave dominated. Moreover, the large cross-section needed to account for the X-ray line requires the large

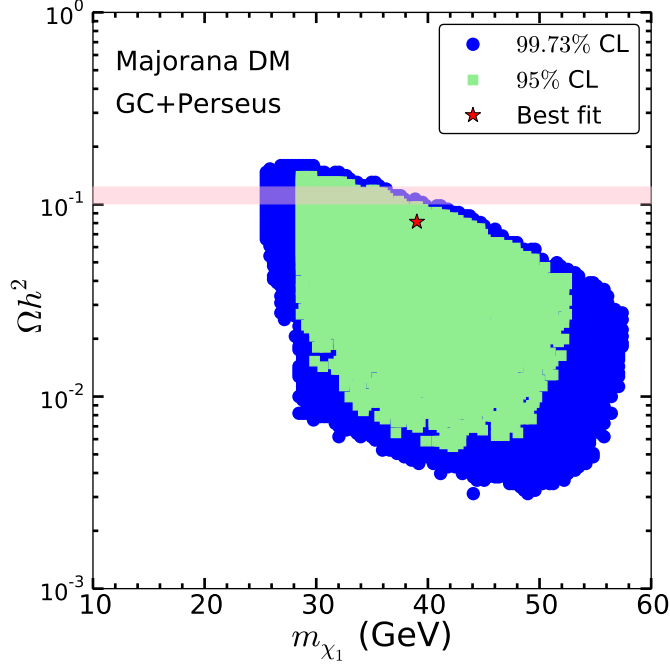


Figure 8: The 95% and 99.73% confidence-level regions in the plane of Ωh^2 versus m_{χ_1} obtained in the fits with γ -ray and X-ray data only in the Majorana DM case. The horizontal band in pink indicates $1\text{-}\sigma$ range (including the theoretical error) of PLANCK measurement on the relic abundance.

resonance enhancement with the help of the very small X^3 decay width. The large DM velocity ($\sim \frac{1}{3}c$) at freeze-out implies a considerable deviation from the resonance when DM decouples from the thermal universe. In order to achieve $\langle\sigma v\rangle_\gamma \sim 10^{-26} \text{ cm}^3\text{sec}^{-1}$ at current time, the cross-section of $\bar{\psi}_1\psi_1 \rightarrow \bar{f}f$ at freeze-out will be much smaller than $3 \times 10^{-26} \text{ cm}^3\text{sec}^{-1}$, the size required to reproduce the DM density. Therefore, we do not include the DM relic density constraint into the fits here. Notice that we have to take into account the stringent bounds on the spin-independent DM-nucleon cross-section [84] due to vector-current interactions, but it hardly has any impact on the analysis since $\sin\chi$ of interest is extremely small, leading to a large suppression on the DM-nucleon cross-section.

In Fig. 9, we show $\langle\sigma v\rangle$ versus m_{ψ_1} for X-rays (left panel) and γ -rays (right panel). Unlike the Majorana case in Fig. 6, the best-fit point in $\langle\sigma v\rangle_{\text{X-ray}}$ is near the central area of the confidence region since g_X is much smaller than that of the Majorana case. The steep shrink on the 2σ confidence region, which is observed at the Majorana case as well, around $m_{\psi_1} \approx 29$ GeV is again due to the sharp change on the GC γ -ray spectrum around 0.5 GeV shown in Fig. 4.

In Fig. 10, we show g_X , $\sin\chi$ and δ versus m_{ψ_1} , respectively. All processes of interest are S -wave dominated without the DM velocity suppression. It implies that the resonance enhancement from the narrow X^3 decay width alone is sufficient to achieve the large $\langle\sigma v\rangle_{\text{X-ray}}$ without resorting to large g_X . Therefore, g_X is of $\mathcal{O}(0.6)$ in this case, compared to $g_X \sim 10$ for Majorana χ_1 . Similar to the Majorana DM case explained above, around $m_{\psi_1} (\simeq m_{X^3}) \approx \frac{1}{2}m_Z$, ζ defined in Eq. (2.13) becomes large, resulting in large $g_{L,R}$ ($\sim \sin\zeta$) and $\langle\sigma v\rangle_\gamma$. It is then offset by the decrease in $\sin\chi$ as shown in the left panel of Fig. 10. At the same time,

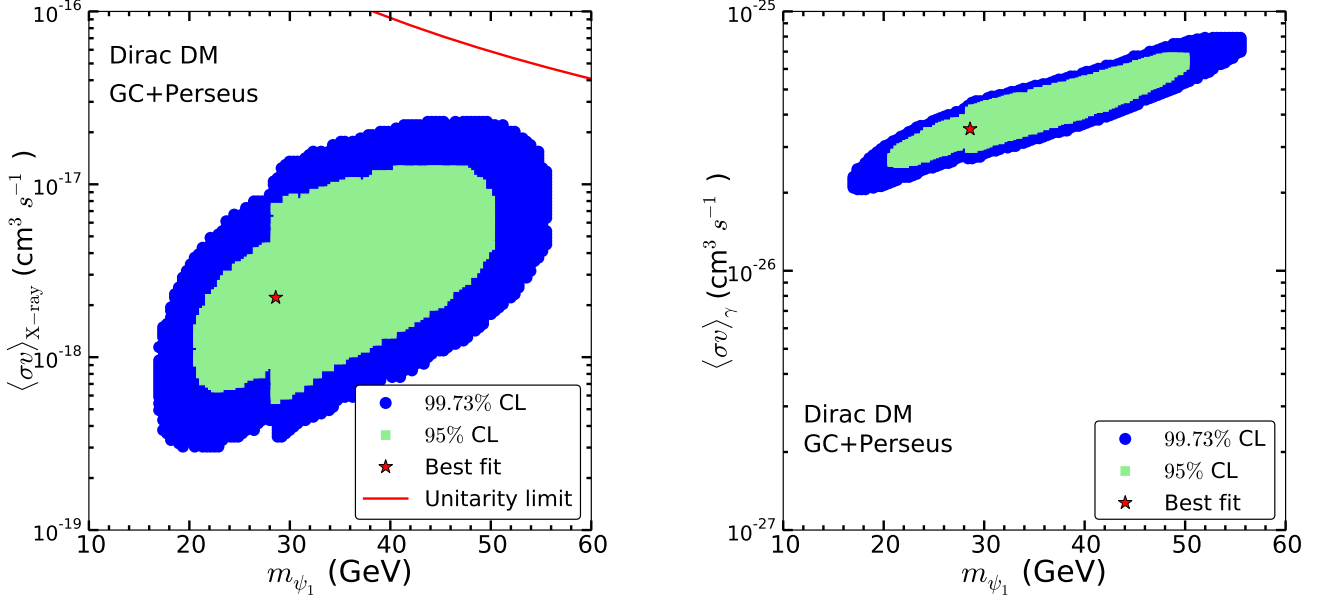


Figure 9: The 95% and 99.73% confidence-level regions in the plane of annihilation cross sections versus the DM mass obtained in the fits with GC gamma-ray and Perseus X-ray data only. for the Dirac DM case. Left panel: $\langle\sigma v\rangle_{X\text{-ray}}$ versus m_{ψ_1} for X-rays; right panel: $\langle\sigma v\rangle_{\gamma}$ versus m_{ψ_1} for γ -rays.

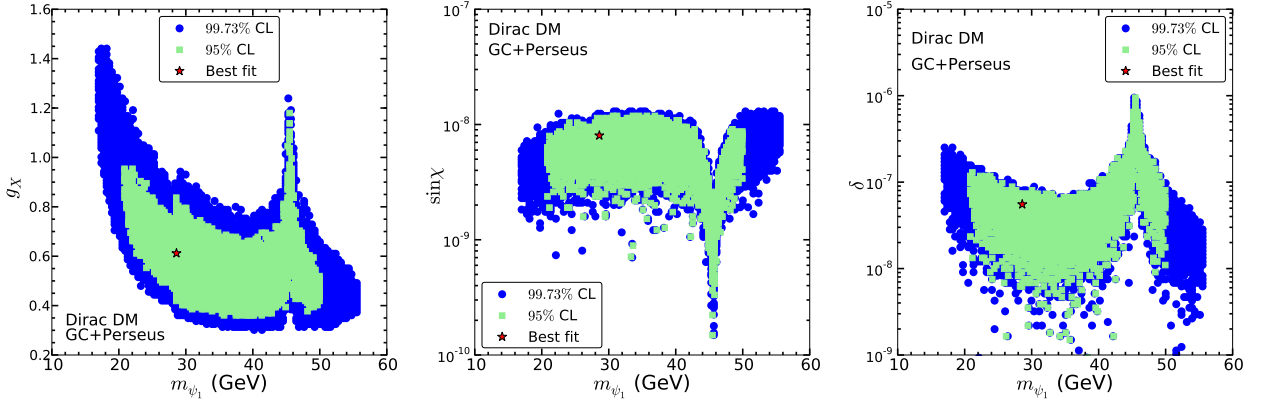


Figure 10: The 95% and 99.73% confidence-level regions in the planes of (m_{χ_1}, g_X) (left panel), $(m_{\chi_1}, \sin\chi)$ (middle), and (m_{χ_1}, δ) (right) obtained in the fits with GC gamma-ray and Perseus X-ray data only in the Dirac DM case.

from Eq. (3.11), large ζ implies that $\langle\sigma v\rangle_{X\text{-ray}} (\sim (g_X \cos\zeta)^4)$ becomes smaller. So g_X has to increase to achieve $\langle\sigma v\rangle_{X\text{-ray}} \sim 10^{-19} \text{ cm}^3 \text{ sec}^{-1}$ for the X-ray line, as seen from the middle panel. In addition, larger g_X implies larger $\langle\sigma v\rangle_{\gamma}$, which can be reduced by larger δ (and a larger deviation away from the resonance region) as in the right-panel.⁸ Note that for the

⁸Again, $\langle\sigma v\rangle_{X\text{-ray}}$ is insensitive to the δ change in the saturated area as shown in Fig. 5.

| DM type | Majorana | | Dirac |
|---|--|--|---|
| constraints | GC+Perseus | GC+Perseus+ $\Omega_{DM}h^2$ | GC+Perseus |
| DM mass (GeV) | 39.01 | 32.32 | 28.6 |
| $\sin \chi$ | 2.2×10^{-7} | 2.9×10^{-7} | 8.0×10^{-9} |
| g_X | 12.56 | 12.43 | 0.61 |
| δ | 1.6×10^{-10} | 1.46×10^{-10} | 5.53×10^{-8} |
| $\chi^2(\text{GC})/p\text{-value}$ | 17.29/63.4% | 16.32/70% | 15.53/74.5% |
| $\chi^2(\text{Perseus})/p\text{-value}$ | 3.36/33.9% | 5.75/12.4% | 0.023/99.99% |
| $\chi^2(\Omega_{DM}h^2)/p\text{-value}$ | 20.40/0.01% | 0.06/99.62% | 100.0/0% |
| 99.73% confidence region | | | |
| m_{χ_1}/m_{ψ_1} (GeV) | [25.36, 57.90] | [24.38, 39.55] | [16.80, 56.11] |
| $\sin \chi$ | $[4.1 \times 10^{-9}, 1.4 \times 10^{-6}]$ | $[2.07 \times 10^{-7}, 3.86 \times 10^{-7}]$ | $[1.45 \times 10^{-10}, 1.39 \times 10^{-8}]$ |
| g_X | [9.48, 4π] | [9.71, 4π] | [0.30, 1.48] |
| δ | $[10^{-10}, 1.29 \times 10^{-7}]$ | $[10^{-10}, 3.59 \times 10^{-9}]$ | $[8.3 \times 10^{-11}, 1.09 \times 10^{-6}]$ |

Table 4: Best fit points of the Majorana and Dirac DM cases with two sets of constraints: GC+Perseus and GC+Perseus+ $\Omega_{DM}h^2$. The best-fit point for the Dirac DM case are the same for two sets of constraints. The p -values are computed based on the degrees of freedom, 3 for Perseus and $\Omega_{DM}h^2$ and 20 for GC.

Majorana case, we do not spot this behavior for g_X and δ since g_X is constrained to be less than 4π .

To summarize, we present in Table 4 the chi-squares (χ^2) and p -values for the best-fit points, and also the 3σ confidence regions for both the Majorana and Dirac DM cases. We would like to emphasize again that first, both cases can explain the γ -ray and X-ray data but only the Majorana DM can reproduce the correct DM density. Second, the best-fit point shifts toward the lower m_{χ_1} region when including the DM relic density into the fits. Finally, g_X is close to 4π in the Majorana case because of P -wave velocity suppression as opposed to the Dirac case where g_X is of $\mathcal{O}(0.6)$.

6 Conclusions

In this work, we have attempted to explain simultaneously the GC γ -ray excess and the 3.5 keV X-ray line, as well as fulfilling the DM relic abundance in the context of non-abelian DM models, and we have success in the case of Majorana DM with a Dirac excited state. We employed a “dark” $SU(2)_X$ gauge group with a $SU(2)_X$ doublet consisting of the DM particle and the excited state with a mass-splitting of 3.5 keV. The $SU(2)_X$ sector talks to the SM gauge groups via kinetic mixing, characterized by $\sin \chi$. We have studied two cases: Majorana DM (χ_1) and Dirac DM (ψ_1), and both with the Dirac excited state ψ_2 . The X-ray line results from $\chi_1\chi_1$ ($\bar{\psi}_1\psi_1$) \rightarrow $\bar{\psi}_2\psi_2$, followed by the decay of ψ_2 back to the DM and a photon. On the other hand, DM annihilations into SM fermions, which then emit photons, can explain the GC γ -ray excess but this process is suppressed by the aforementioned $SU(2)_X$ -SM kinetic mixing. In order to account for the γ - and X-ray data, one would need $\langle\sigma v\rangle_{X\text{-ray}} \sim 10^{-19}$ and $\langle\sigma v\rangle_\gamma \sim 10^{-26} \text{ cm}^3\text{sec}^{-1}$. We employ the resonance enhancement to fulfill the large $\langle\sigma v\rangle_{X\text{-ray}}$. Additionally, the large hierarchy between two cross-sections $\langle\sigma v\rangle_{X\text{-ray}}/\langle\sigma v\rangle_\gamma$ ($\sim 10^7$) can be

realized if the kinetic mixing is very small ($\sin \chi \lesssim 10^{-7}$).

For the Majorana DM case, both the γ -ray and X -ray excess can be accommodated really well. However, all χ_1 -involved processes are P -wave suppressed due to the Majorana nature. As a result, the $SU(2)_X$ gauge coupling g_X is driven close to the perturbativity limit 4π to counterbalance the velocity suppression. Regarding the DM relic density, the relatively large DM velocity ($\sim \frac{1}{3}c$) at freeze-out compared to the current one ($\sim 10^{-3}c$) implies a large deviation from the resonance region. Therefore, the cross-section of $\chi_1\chi_1 \rightarrow \bar{f}f$ at freeze-out is much smaller than the current value $10^{-26} \text{ cm}^3\text{sec}^{-1}$ demanded to explain the GC γ -ray excess, as well as much smaller than $3 \times 10^{-26} \text{ cm}^3\text{sec}^{-1}$, the size of the cross section to achieve the correct relic density. The solution comes from the S -wave dominated process $\bar{\psi}_2\psi_2 \rightarrow \bar{f}f$, which should be included as an coannihilation process at the freeze-out in light of the tiny mass splitting between χ_1 and ψ_2 . The coannihilation can reach a level of $3 \times 10^{-26} \text{ cm}^3\text{sec}^{-1}$ for certain m_{ψ_2} to reproduce the correct relic density. The allowed m_{χ_1} (also m_{ψ_2}) ranges from 25 to 40 GeV. This coannihilation cross section is much larger than the cross section of the P -wave process $\chi_1\chi_1 \rightarrow \bar{f}f$.

In the Dirac DM case, the model can explain both γ - and X -ray data for $16 \lesssim m_{\psi_1} \lesssim 56$ GeV, with much smaller g_X (~ 0.6) compared to the Majorana DM case, since all processes involved are S -wave dominated without the velocity suppression. Nevertheless, it cannot yield the proper DM relic density because both ψ_1 and ψ_2 annihilations into SM fermions are of the same order at freeze-out and both annihilations are away from the resonance region due to the large DM velocity. As a consequence, they are much smaller than $10^{-26} \text{ cm}^3\text{sec}^{-1}$, the current value for $\bar{\psi}_1\psi_1 \rightarrow \bar{f}f$, associated with the GC γ -ray. An additional mechanism has to be introduced to increase the annihilation cross-section and lower the relic density. In addition, the direct search bounds hardly constrain our model since the $SU(2)_X$ -SM mixing $\sin \chi$ is very small such that the DM-nucleon cross-section is negligible.

It is worthwhile to mention that recent studies [85–87], based on the AMS-02 electron and positron data [88, 89], infer stringent bounds on low-mass DM annihilation into leptons and also quarks. In these works, the background with broken power-laws in energy fits the data very well, leading to strong constraints on the DM component. It might be arguable that the broken power-law background is driven by the AMS02 data and somehow different from the conventional background. Hence, we take a more conservative point of view that as long as predicted DM signals do not exceed the AMS-02 data. In this sense, such approach is not able to constrain our model.

Finally, we would like to comment that we have taken a phenomenological approach, without justifying the smallness of the mass splitting between the DM and the excited state, as well as and the tiny kinetic mixing. Both are basically determined based on the γ - and X -ray data. Besides, as shown in Table 4 for the 99.73% confidence region, the resonance condition of $m_{X^3} \simeq 2m_{\chi_1}$ has to be precisely satisfied up to one part in 10^9 or 10^6 for the Majorana or Dirac case respectively, where δ is driven to 10^{-9} for the strong enhancement on the (co-)annihilation cross-section of the excited state to achieve the correct density in the Majorana case. This fine-tuning results from the hierarchical annihilations required to explain

the X-ray line and GC γ -ray excess and it could arise from an underlying flavor symmetry, aligned with the gauge symmetry such that the resonance is not perturbed by large gauge couplings. The concrete model building is, however, beyond the scope of this work.

Acknowledgments

We would like to thank Andrew Frey for useful discussions. W. C. Huang is grateful for the hospitality of CERN theory group and AHEP group in IFIC, where part of this work was performed. This work is partially supported by the London Centre for Terauniverse Studies (LCTS), using funding from the European Research Council via the Advanced Investigator Grant 267352, and in part by the MoST of Taiwan under Grant No. NSC 102-2112-M-007-015-MY3. Y. Tsai was supported by World Premier International Research Center Initiative (WPI), MEXT, Japan.

A Resonance enhancement and cancellation

We here show that if both the DM and the excited state are Majorana particles and degenerate in mass, one cannot obtain the resonance enhancement but the “resonance cancellation” instead. So it is not capable of achieving the required large cross-section for the X-ray line. For demonstration, we use the following two types of interactions, the vector current and axial-vector current, for purely Dirac and Majorana DM:

$$\begin{aligned}\mathcal{L}_M &\supset \sum_{i=1}^2 g_X \chi_i^\dagger \bar{\sigma}^\mu \chi_i X_\mu, \\ \mathcal{L}_D &\supset \sum_{i=1}^2 g_X \bar{\psi}_i \gamma^\mu \psi_i X_\mu,\end{aligned}\tag{A.1}$$

where $i = 1$ (2) corresponds to DM (excited state) with χ (ψ) referring to a Majorana (Dirac) particle.

In the vicinity of the resonance ($2m_{\chi(\psi)_1} \sim m_X$) and the low DM velocity $v \ll c$, the resulting cross-sections for $\chi_1 \chi_1 \rightarrow \chi_2 \chi_2$ and $\bar{\psi}_1 \psi_1 \rightarrow \bar{\psi}_2 \psi_2$ through the current interactions read

$$\begin{aligned}(\sigma v)_{\chi_1 \chi_1 \rightarrow \chi_2 \chi_2} &\sim \frac{(m_{\chi_1}^8 - m_{\chi_1}^6 m_{\chi_2}^2) v^2 + 12 m_{\chi_1}^4 m_{\chi_1}^2 (m_X - 2m_{\chi_1})^2}{m_X^4 \left((s - m_X^2)^2 + \Gamma_X^2 m_X^2 \right)}, \\ (\sigma v)_{\bar{\psi}_1 \psi_1 \rightarrow \bar{\psi}_2 \psi_2} &\sim \frac{2m_{\psi_1}^4 + m_{\psi_1}^2 m_{\psi_2}^2}{\left((s - m_X^2)^2 + \Gamma_X^2 m_X^2 \right)},\end{aligned}\tag{A.2}$$

where we have suppressed coupling constants and coefficients from the phase space integral and kinematics. For the Majorana case, the first term in the numerator is double suppressed because of $v \ll 1$ and $m_{\chi_1} \simeq m_{\psi_2}$ and the second term becomes small in the vicinity of the

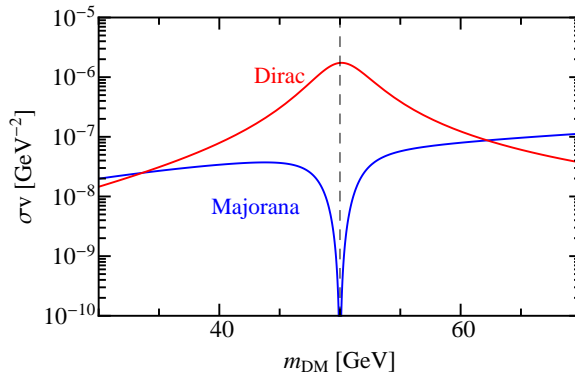


Figure 11: *The cross-section for the purely Majorana case (blue) and Dirac case (red). We assume a 3.5 keV mass splitting between DM and the excited state, $\Gamma_X = \frac{m_X}{10} = 10$ GeV and $v \sim 3 \times 10^{-3} c$.*

resonance. In contrast, in the Dirac case the numerator is unsuppressed, which is characteristic of S -wave. In Fig. 11, we show the comparison between the two cases, in which we assume a 3.5 keV mass splitting between the DM and the excited state, $\Gamma_X = \frac{m_X}{10} = 10$ GeV, and $v \sim 3 \times 10^{-3} c$. It is clear that the pure Majorana case has the resonance “cancellation” instead of enhancement while the S -wave Dirac case features the resonance behavior as expected.

References

- [1] Fermi-LAT Collaboration, M. Ackermann *et al.*, *Astrophys.J.* (2014), 1407.7905.
- [2] L. Goodenough and D. Hooper, (2009), 0910.2998.
- [3] D. Hooper and L. Goodenough, *Phys.Lett.* **B697**, 412 (2011), 1010.2752.
- [4] A. Boyarsky, D. Malyshev, and O. Ruchayskiy, *Phys.Lett.* **B705**, 165 (2011), 1012.5839.
- [5] K. N. Abazajian and M. Kaplinghat, *Phys.Rev.* **D86**, 083511 (2012), 1207.6047.
- [6] C. Gordon and O. Macias, *Phys.Rev.* **D88**, 083521 (2013), 1306.5725.
- [7] W.-C. Huang, A. Urbano, and W. Xue, *JCAP* **1404**, 020 (2014), 1310.7609.
- [8] N. Okada and O. Seto, *Phys.Rev.* **D89**, 043525 (2014), 1310.5991.
- [9] K. P. Modak, D. Majumdar, and S. Rakshit, *JCAP* **1503**, 011 (2015), 1312.7488.
- [10] K. N. Abazajian, N. Canac, S. Horiuchi, and M. Kaplinghat, *Phys.Rev.* **D90**, 023526 (2014), 1402.4090.
- [11] T. Daylan *et al.*, (2014), 1402.6703.

- [12] T. Lacroix, C. Boehm, and J. Silk, Phys.Rev. **D90**, 043508 (2014), 1403.1987.
- [13] N. Okada and O. Seto, Phys.Rev. **D90**, 083523 (2014), 1408.2583.
- [14] B. Zhou *et al.*, (2014), 1406.6948.
- [15] L. Wang, (2014), 1406.3598.
- [16] E. Bulbul *et al.*, Astrophys.J. **789**, 13 (2014), 1402.2301.
- [17] A. Boyarsky, O. Ruchayskiy, D. Iakubovskiy, and J. Franse, (2014), 1402.4119.
- [18] J. M. Cline and A. R. Frey, (2014), 1408.0233.
- [19] K. N. Abazajian, Phys.Rev.Lett. **112**, 161303 (2014), 1403.0954.
- [20] A. Adulpravitchai and M. A. Schmidt, (2014), 1409.4330.
- [21] S. Baek, P. Ko, and W.-I. Park, (2014), 1405.3730.
- [22] S. Baek and H. Okada, (2014), 1403.1710.
- [23] K. Babu and R. N. Mohapatra, Phys.Rev. **D89**, 115011 (2014), 1404.2220.
- [24] F. Bezrukov and D. Gorbunov, Phys.Lett. **B736**, 494 (2014), 1403.4638.
- [25] K. K. Boddy, J. L. Feng, M. Kaplinghat, Y. Shadmi, and T. M. P. Tait, (2014), 1408.6532.
- [26] N. E. Bomark and L. Roszkowski, Phys.Rev. **D90**, 011701 (2014), 1403.6503.
- [27] S. Chakraborty, D. K. Ghosh, and S. Roy, (2014), 1405.6967.
- [28] N. Chen, Z. Liu, and P. Nath, (2014), 1406.0687.
- [29] C.-W. Chiang and T. Yamada, JHEP **1409**, 006 (2014), 1407.0460.
- [30] K.-Y. Choi and O. Seto, Phys.Lett. **B735**, 92 (2014), 1403.1782.
- [31] M. Cicoli, J. P. Conlon, M. C. D. Marsh, and M. Rummel, Phys.Rev. **D90**, 023540 (2014), 1403.2370.
- [32] J. M. Cline, Y. Farzan, Z. Liu, G. D. Moore, and W. Xue, Phys.Rev. **D89**, 121302 (2014), 1404.3729.
- [33] J. P. Conlon and F. V. Day, (2014), 1404.7741.
- [34] J. P. Conlon and A. J. Powell, (2014), 1406.5518.
- [35] V. Dubrovich, (2014), 1407.4629.

- [36] E. Dudas, L. Heurtier, and Y. Mambrini, Phys.Rev. **D90**, 035002 (2014), 1404.1927.
- [37] R. Allahverdi, B. Dutta, and Y. Gao, Phys.Rev. **D89**, 127305 (2014), 1403.5717.
- [38] B. Dutta, I. Gogoladze, R. Khalid, and Q. Shafi, (2014), 1407.0863.
- [39] D. P. Finkbeiner and N. Weiner, (2014), 1402.6671.
- [40] M. T. Frandsen, F. Sannino, I. M. Shoemaker, and O. Svendsen, JCAP **1405**, 033 (2014), 1403.1570.
- [41] M. Frigerio and C. E. Yaguna, (2014), 1409.0659.
- [42] Y. Farzan and A. R. Akbarieh, (2014), 1408.2950.
- [43] G. Faisel, S.-Y. Ho, and J. Tandean, (2014), 1408.5887.
- [44] C.-Q. Geng, D. Huang, and L.-H. Tsai, JHEP **1408**, 086 (2014), 1406.6481.
- [45] N. Haba, H. Ishida, and R. Takahashi, (2014), 1407.6827.
- [46] T. Higaki, K. S. Jeong, and F. Takahashi, Phys.Lett. **B733**, 25 (2014), 1402.6965.
- [47] T. Higaki, N. Kitajima, and F. Takahashi, (2014), 1408.3936.
- [48] H. Ishida, K. S. Jeong, and F. Takahashi, Phys.Lett. **B732**, 196 (2014), 1402.5837.
- [49] H. Ishida and H. Okada, (2014), 1406.5808.
- [50] J. Jaeckel, J. Redondo, and A. Ringwald, Phys.Rev. **D89**, 103511 (2014), 1402.7335.
- [51] J.-C. Park, S. C. Park, and K. Kong, Phys.Lett. **B733**, 217 (2014), 1403.1536.
- [52] C. Kolda and J. Unwin, Phys.Rev. **D90**, 023535 (2014), 1403.5580.
- [53] Z. Kang, P. Ko, T. Li, and Y. Liu, (2014), 1403.7742.
- [54] H. M. Lee, (2014), 1404.5446.
- [55] S. P. Liew, JCAP **1405**, 044 (2014), 1403.6621.
- [56] K. P. Modak, (2014), 1404.3676.
- [57] K. Nakayama, F. Takahashi, and T. T. Yanagida, Phys.Lett. **B735**, 338 (2014), 1403.1733.
- [58] K. Nakayama, F. Takahashi, and T. T. Yanagida, Phys.Lett. **B734**, 178 (2014), 1403.7390.

- [59] K. Nakayama, F. Takahashi, and T. T. Yanagida, Phys.Lett. **B737**, 311 (2014), 1405.4670.
- [60] H. Okada and Y. Orikasa, (2014), 1407.2543.
- [61] H. Okada and T. Toma, Phys.Lett. **B737**, 162 (2014), 1404.4795.
- [62] S. Patra and P. Pritimita, (2014), 1409.3656.
- [63] F. S. Queiroz and K. Sinha, Phys.Lett. **B735**, 69 (2014), 1404.1400.
- [64] D. J. Robinson and Y. Tsai, Phys.Rev. **D90**, 045030 (2014), 1404.7118.
- [65] W. Rodejohann and H. Zhang, Phys.Lett. **B737**, 81 (2014), 1407.2739.
- [66] J. M. Cline and A. R. Frey, Phys.Rev. **D90**, 123537 (2014), 1410.7766.
- [67] F. Chen, J. M. Cline, and A. R. Frey, Phys.Rev. **D80**, 083516 (2009), 0907.4746.
- [68] J. Knodlseder *et al.*, Astron.Astrophys. **441**, 513 (2005), astro-ph/0506026.
- [69] C. Boehm *et al.*, (2014), 1406.4683.
- [70] S. Cassel, D. Ghilencea, and G. Ross, Nucl.Phys. **B827**, 256 (2010), 0903.1118.
- [71] F. Ferrer and D. R. Hunter, JCAP **1309**, 005 (2013), 1306.6586.
- [72] J. F. Navarro, C. S. Frenk, and S. D. White, Astrophys.J. **490**, 493 (1997), astro-ph/9611107.
- [73] H. Zhao, Mon.Not.Roy.Astron.Soc. **278**, 488 (1996), astro-ph/9509122.
- [74] D. Hooper and T. R. Slatyer, Phys.Dark Univ. **2**, 118 (2013), 1302.6589.
- [75] M. Fornasa and A. M. Green, Phys.Rev. **D89**, 063531 (2014), 1311.5477.
- [76] M. Cirelli *et al.*, JCAP **1103**, 051 (2011), 1012.4515.
- [77] F. Calore, I. Cholis, and C. Weniger, (2014), 1409.0042.
- [78] D. T. Cumberbatch, Y.-L. S. Tsai, and L. Roszkowski, Phys.Rev. **D82**, 103521 (2010), 1003.2808.
- [79] K. Griest and D. Seckel, Phys.Rev. **D43**, 3191 (1991).
- [80] P. Gondolo *et al.*, JCAP **0407**, 008 (2004), astro-ph/0406204.
- [81] Planck Collaboration, P. Ade *et al.*, Astron.Astrophys. (2014), 1303.5076.
- [82] K. Griest and M. Kamionkowski, Phys.Rev.Lett. **64**, 615 (1990).

- [83] A. Hook, E. Izaguirre, and J. G. Wacker, *Adv.High Energy Phys.* **2011**, 859762 (2011), 1006.0973.
- [84] LUX Collaboration, D. Akerib *et al.*, *Phys.Rev.Lett.* **112**, 091303 (2014), 1310.8214.
- [85] L. Bergstrom, T. Bringmann, I. Cholis, D. Hooper, and C. Weniger, *Phys.Rev.Lett.* **111**, 171101 (2013), 1306.3983.
- [86] A. Ibarra, A. S. Lamperstorfer, and J. Silk, *Phys.Rev.* **D89**, 063539 (2014), 1309.2570.
- [87] K. Kong and J.-C. Park, *Nucl.Phys.* **B888**, 154 (2014), 1404.3741.
- [88] AMS Collaboration, M. Aguilar *et al.*, *Phys.Rev.Lett.* **110**, 141102 (2013).
- [89] AMS Collaboration, L. Accardo *et al.*, *Phys.Rev.Lett.* **113**, 121101 (2014).